

Novel molecular architectures for “multicolor” magnetic resonance imaging

<https://doi.org/10.51167/ice000017>

Amnon Bar-Shir

Department of Molecular Chemistry and Materials Science, Weizmann Institute of Science, Rehovot, 7610001, Israel

Email: amnon.barshir@weizmann.ac.il

Abstract:

Luminescent materials with their rich color palettes have revolutionized the field of bioimaging through the ability to distinguish between spectrally resolved colors and, thus, to map the complexity of biological systems. Yet, advanced solutions to overcome the restricted tissue penetration of light are still needed to allow in vivo mapping of tissue multiplexity in both health and disease. Among the diverse capabilities and many advantages of MRI, the ability to encode specific frequencies of imaging agents and, by that, to allow pseudo-color display of MRI maps, is unique. Here, I summarize our recently developed molecular probes that are capable of generating artificial MR-based colors. To this end, the use of nanofabrication, supramolecular chemistry, and protein engineering approaches to generate novel molecular formulations (inorganic nanocrystals, supramolecular assemblies, and enzyme/substrate pairs) as MRI sensors with unique multicolor display characteristics is reviewed.

1. Introduction

The complexity of biological processes, as well as their tightly controlled regulation, attracts researchers from a wide range of scientific fields. Such multiplexity is apparent in almost every aspect of life, in health and in disease, from enzymatic activity to protein-protein interactions, from metal ion homeostasis to cell function, from gene expression to neuronal activity, or from gene networks to disease onset and therapeutics mechanisms. Although our accumulated knowledge allows us to understand many aspects of these processes, some are still elusive, unknown, or cannot be studied in an intact live organism. In this regard, luminescent sensors (small molecules [1], proteins [2], or nanoformulations [3]) have been the “highlighter pens” of science for decades, since they enable molecules (or cells) of interest to be tagged,

enabling mapping of their location, levels, and functions in multiple distinguishable colors. This capability has advanced our ability to reveal the complexity of cellular events, study their tight regulation, and explore a wide range of biological processes concurrently. Perfecting the chemical and optical properties of luminescent materials, in addition to dramatic improvements in microscopy technologies, provide scientists with the ability to visualize multiple biological targets simultaneously within the same imaging frame. However, the light signal source of these materials remains an obstacle when information is desired from the deep tissue of a live subject.

MRI, with its unlimited tissue penetration capabilities and ability to combine information from biological targets with high-resolution anatomical images, has become a valuable imaging technology for molecular and cellular imaging.

Amnon Bar-Shir earned his BSc (2002) and MSc in chemistry from Tel Aviv University (2004, under Michael Gozin), both magna cum laude. His PhD (2009, under Yoram Cohen) focused on advanced diffusion NMR and MRI to study the structure and function of the central nervous system. As a postdoc at the Johns Hopkins University School of Medicine under Assaf Gilad he developed genetically engineered reporters for MRI. In 2014 he joined the Weizmann Institute, where he created new kinds of biosensors with artificial “multicolor” features for MRI applications. His lab uses synthetic chemistry, nanofabrication, and protein engineering to generate novel molecular formulations, such as small molecules, nanocrystals, supramolecular assemblies and proteins, as MRI sensors of high sensitivity, specificity, and orthogonality. He has used these methods for in-vivo molecular and cellular MRI studies for mapping inflammation, multiplexed in-vivo MRI, imaging orthogonal reporter genes, and sensing metal ions. In addition, he used his techniques to study fundamental questions in supramolecular chemistry, including kinetic features of dynamically exchanging molecular systems and control over nanocrystal formation. Amnon’s research achievements were recognized recently by the 2019 Krill Prize, and the 2021 ICS Excellent Young Scientist Prize.



Moreover, the versatility of MRI contrast mechanisms [4, 5], and the variability in imaging probe identities (including non- ^1H tracers), create many possibilities for the design of MRI sensors. One feature that is unique to MRI is that this technique relies on MR properties, which allows, among other advantages, differentiation between molecular entities based on their chemical environment, which is reflected by a characteristic chemical shift. If spectrally resolved, the frequencies of multiple chemical shifts of properly designed molecular probes can be exploited for multiplexed imaging by introducing MRI maps with pseudo-color features [6, 7]. Such pseudo-MRI-colors can be generated using several strategies, including the use of non- ^1H nuclei, which frequently provide improved spectral resolution, or through magnetization transfer mechanisms that benefit from the high sensitivity of ^1H -MRI. In recent years, our lab has focused on the development of novel molecular formulations of a variety of

types, as well as on developing methods for pseudo-color *in vivo* MR imaging. I here provide an overview of our recent developments, emphasizing the newly proposed MRI sensors that are based on inorganic nanocrystals (NCs), host-guest systems, and engineered proteins, which have the potential to extend the MRI toolbox with features that have been, thus far, inaccessible.

Principles of generating pseudo-colors for MRI

Several strategies have been proposed to generate pseudo-colors for MRI applications. One example is the use of the chemical exchange saturation transfer (CEST) contrast mechanism to produce artificial MRI colors (Figure 1a). By applying a saturation pulse at the specific resonance of an exchangeable proton of a putative CEST agent, it can be “tagged.” This tag (manifested by its MR signal nullification) is transferred to the water protons in the surrounding area and leads to ^1H -MRI signal reduction as a result of the dynamic exchange process of the “tagged” protons with the water protons. Using multiple CEST agents with exchangeable protons that resonate at different and specific chemical shift offsets ($\Delta\omega$ s) from the resonance of the water protons (set at 0.0), artificial MRI colors can be generated, as demonstrated for several applications [6, 8]. The relatively large chemical shift range of fluorinated materials in a ^{19}F -MR framework was also exploited for spectral differentiation between different fabrications and presents this range in a pseudo-color manner (Figure 1b) [7, 9, 10]. Benefitting from the negligible tissue background in ^{19}F -MRI and the ^{19}F -MR signal quantifiability, multicolor ^{19}F -MRI studies provide unique multicolor MRI features that are not accessible to a ^1H -CEST-based approach. Combining the two strategies for multicolor MRI, i.e., CEST and ^{19}F -MR to obtain ^{19}F -CEST [11] (Figure 1c), provides a novel MRI platform that can be implemented for applications in which both ^1H -CEST and ^{19}F -MRI are not applicable.

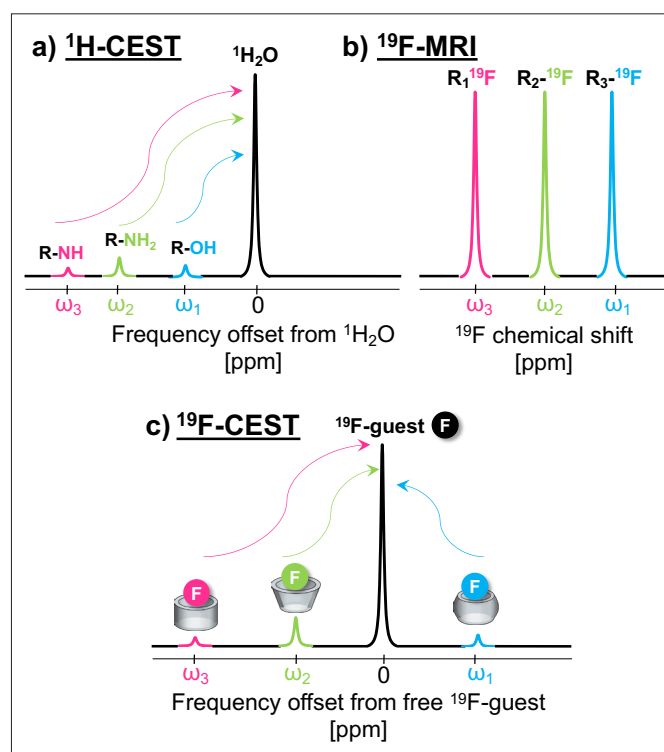


Figure 1. Strategies to generate artificial colors in ^1H - and ^{19}F -MRI frameworks. (a) Artificial colors can be generated in CEST-MRI by exploiting the different chemical shift offsets of different exchangeable protons of ^1H -CEST agents. (b) In ^{19}F -MRI, artificial colors can be generated by using different ^{19}F -agents based on the difference in the ^{19}F -chemical shifts of their fluorinated content. (c) In the ^{19}F -CEST approach, which is applied on host-guest systems (termed guest exchange saturation transfer, GEST), the same principles used to generate artificial colors in ^1H -CEST are used. In this case, the different chemical shift offsets are obtained from the complexation of a ^{19}F -guest with a different molecular host in the solution.

Nanofluorides

Fluorine-19 is the second most NMR-sensitive nucleus (after ^1H) and is therefore favorable for MR-based studies (NMR and MRI) and fluorinated materials have been proposed as ^{19}F -MR imaging tracers [12], overcoming some of the major drawbacks (i.e., strong background signal, non-quantifiable, challenging in multiplexing, etc.) of paramagnetic contrast agents. Combining this with the fact that ^{19}F -nuclei do not exist in soft biological tissues, the ^{19}F -MR signal of an introduced ^{19}F -tracer can be directly monitored and presented

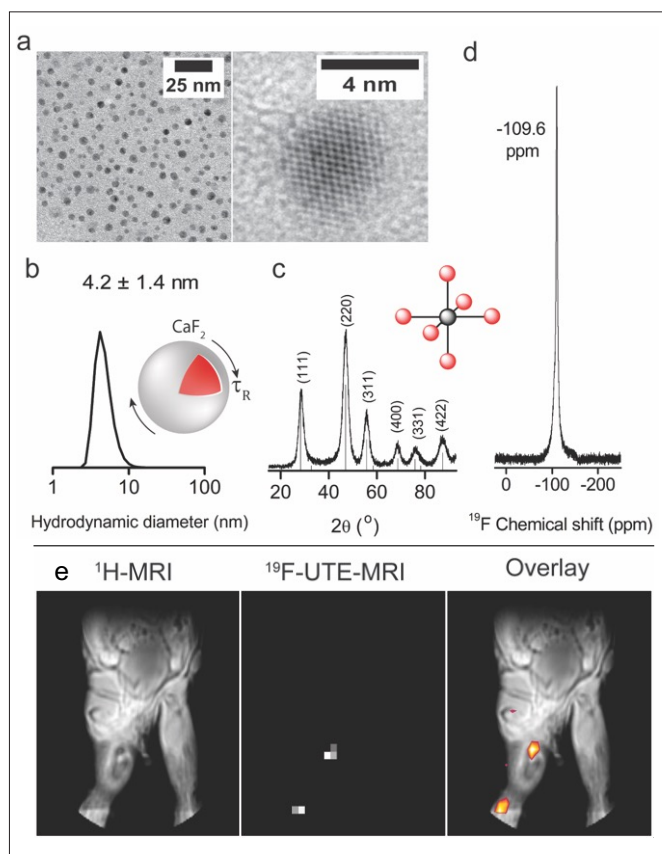


Figure 2. ^{19}F -NMR and ^{19}F -MRI of water-soluble CaF_2 NCs. (a) TEM images. (b) DLS histogram. (c) XRD pattern with schematic of the Ca^{2+} first coordination sphere (red spheres represent ^{19}F -atoms). (d) High-resolution ^{19}F -NMR in water. (e) *In vivo* imaging of PEGylated CaF_2 showing anatomical ^1H -MRI of a representative mouse (left) and matched ^{19}F -MRI (middle) shown as a pseudo-color map overlaid on ^1H -MRI (right). Modified from reference 15 with permission.

as a quantitative “hot-spot” map over anatomical ^1H -MRI. In this regard, perfluorocarbons (PFCs), fluorine-rich materials, have been successfully used in a wide range of ^{19}F -MRI applications [12, 13], including clinical setups [14]. Relying on the relatively large range of their chemical shift appearances in the ^{19}F -NMR spectrum (a few tens of ppm), PFCs have been proposed for multiplexed *in vivo* ^{19}F -MRI [7, 9, 10]. Nevertheless, their introduction as emulsions of a typical 100–200 nm size (i.e., PFC nanoemulsions) and because they are organic formulations, PFC nanoemulsions are not applicable for studies for which ultrasmall (<10 nm) nanoformulations are desired, and they lack the well-established and diverse chemistries of inorganic nanocrystals (NCs). Moreover, they do not cover the whole range of ^{19}F -NMR chemical shifts, which span over almost 200 ppm when using inorganic fluorides (as shown by solid-state NMR).

An inorganic, small-size alternative to PFC nanoemulsions may, therefore, be fluoride-based NCs (M_xF_y , $\text{M} = \text{metal ion}$, $\text{F} = \text{F}^-$), which had not been studied in solutions with high-resolution ^{19}F -NMR and were not used in ^{19}F -MRI until very recently. This is because in NC-based formulations, the restricted mobility of the elements within the crystal frequently results in NMR line-broadening, and high-resolution NMR signals from the core of the NCs’ nuclei cannot be obtained using liquid-state NMR experiments. Overcoming such limitations and, thus, successfully performing liquid-state ^{19}F -NMR experiments of M_xF_y in solution, we offered a novel kind of ^{19}F -nanotracers for ^{19}F -MR imaging, which are based, for the first time, on inorganic fluoride NCs, namely nanofluorides [15]. These nanofluorides combine the advantages of inorganic NCs (e.g., small and controllable sizes, dense fluoride content, monodispersity, colloidal stability, surface modifiability, designed as non-spherical materials, etc.) with the merits of ^{19}F -MRI. In addition, the large chemical shifts of nanofluorides, which can span over almost 200 ppm, provide a platform for the development of a series of fluoride-based NCs with different ^{19}F -NMR chemical shifts, which can serve as artificial “multicolor” tracers for multiplexed MRI.

Demonstrating that high-resolution ^{19}F -NMR spectra can be achieved by sufficient averaging of homonuclear dipolar interactions of ^{19}F -nuclear spins within small-size fluoride-containing NCs (i.e., nanofluorides), we showed that CaF_2 NCs can be used as nano-sized molecular tracers for ^{19}F -MRI [15]. First, small, water-dispersed CaF_2 NCs were synthesized and found to be highly crystalline and monodispersed (Figure 2a) with preserved monodispersity in water, as determined by dynamic light scattering (DLS, Figure 2b). The XRD pattern of the synthetic CaF_2 NCs (Figure 2c) features a typical cubic-phase, fluorite-type, fcc structure, where all fluorides are expected to be magnetically equivalent, as reflected by the first coordination sphere scheme (inset, Figure 2c). Indeed, a singlet peak was observed in the high-resolution ^{19}F -NMR spectrum of water-dispersed CaF_2 NCs at -109 ppm (Figure 2d), similar to the frequency obtained for CaF_2 powder with solid-state NMR [16]. Then, the potential of using the proposed CaF_2 NCs as imaging tracers for *in vivo* ^{19}F -MRI was evaluated in a mouse model of inflammation. To this end, polyethylene-glycol (PEG)-coated CaF_2 NCs were injected into a group of inflamed mice. A clear ^{19}F -MRI signal was observed at the region of the popliteal lymph node of NC-injected mice in the same leg as the injection site (Figure 2e) one hour post-injection.

Although their potential to be used *in vivo* was evident, the T_1 relaxation times of nanofluorides are relatively long (>10 sec) [15], which limits signal averaging and, thus, the signal-to-noise ratio (SNR) in ^{19}F -MR images at a given imaging time.

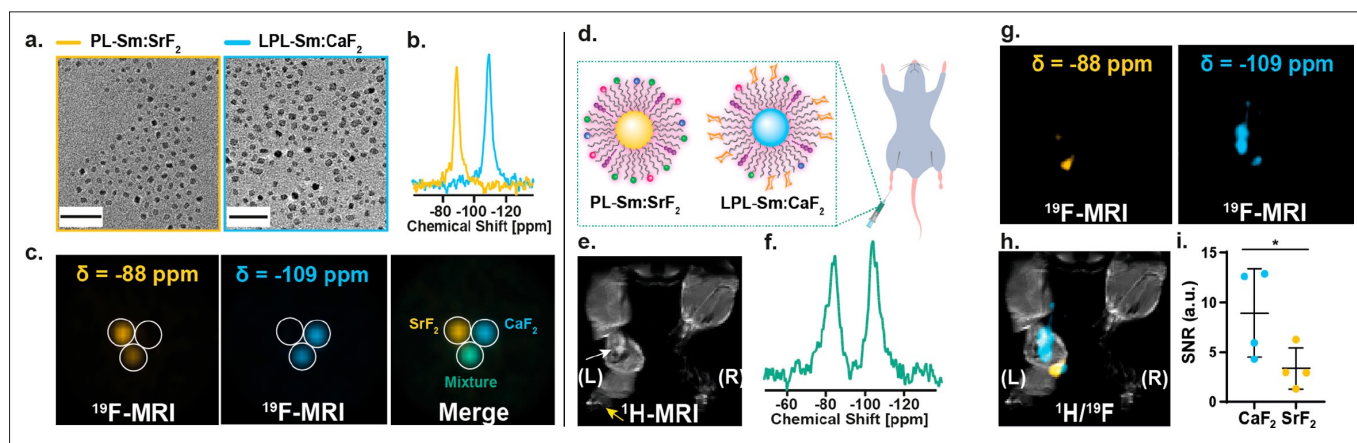


Figure 3. Multicolor ^{19}F -MRI with nanofluorides. (a) TEM images (scale bar: 50 nm) of $\text{Sm}:\text{SrF}_2$ and $\text{Sm}:\text{CaF}_2$ nanofluorides and (b) their ^{19}F -NMR spectra when dispersed in water. (c) Multicolor ^{19}F -MRI of a phantom containing SrF_2 , CaF_2 , or a mixture of these. (d) Schematic representation of nonglycosylated PL-Sm: SrF_2 and glycosylated LPL-Sm: CaF_2 NCs injected as a mixture into the footpad of an inflamed mouse. (e) ^1H -MRI of the inflamed mouse; white arrow indicates the inflamed lymph node, and yellow arrow represents the injection site. (f) *In vivo* ^{19}F -NMR spectrum (total injected PL-Sm: SrF_2 and LPL-Sm: CaF_2). (g) ^{19}F -MRI acquired with the center of the frequency offset set at either -88 ppm (left, yellow) or -109 ppm (right, light blue). (h) Representative $^1\text{H}/^{19}\text{F}$ MRI showing the higher accumulation of LPL-Sm: CaF_2 NCs in the LN. (i) Dot graph presenting the ^{19}F -MRI signal of either PL-Sm: SrF_2 or LPL-Sm: CaF_2 in the lymph node ROI ($n = 4$, Student's *t* test, * represents a p value < 0.05). Scale bar: 50 nm. Modified with permission from ref. 17

<https://pubs.acs.org/doi/10.1021/acsnano.1c01040>

To overcome this pitfall, nanofluorides were doped through their fabrication with the paramagnetic dopant Sm^{3+} , which induced a significant paramagnetic relaxation enhancement (PRE) effect. Specifically, the T_1 of nanofluorides was shortened more than 200-fold, from a T_1 of ca. 15 s for non-doped CaF_2 to an ultrashort T_1 of 70 ms for $\text{Sm}:\text{CaF}_2$ resulting in an eight-fold enhancement in their ^{19}F -MRI SNR [17]. Then, with the introduction of paramagnetic nanofluorides (with $\text{Sm}:\text{CaF}_2$ as a putative example), the ability to classify different types of synthetic nanofluorides and present them in a “multicolor” fashion was also examined. In this regard, the large range of chemical shifts of nanofluorides, which spans from BaF_2 (ca. -10 ppm) to MgF_2 (ca. -200 ppm) [16], provided a platform for the development of a series of fluoride-based NCs with different ^{19}F -NMR chemical shifts. To demonstrate this ability, paramagnetic nanofluorides of the $\text{Sm}:\text{SrF}_2$ type were synthesized to have a size and shape similar to $\text{Sm}:\text{CaF}_2$ (Figure 3a). Dispersed in water, well-resolved, high-resolution ^{19}F NMR peaks that differed from one another by more than ~ 20 ppm (Figure 3b) were obtained with the expected characteristic resonances for SrF_2 (-88 ppm) and CaF_2 (-109 ppm). Such relatively large difference in their chemical shifts allowed spatial mapping of the two types of nanofluorides ($\text{Sm}:\text{CaF}_2$ vs. $\text{Sm}:\text{SrF}_2$) in the same imaging frame, without overlapping signals and without affecting the two detectable ^{19}F -MRI signals (Figure 3c). Specifically, we demonstrated the immune specificity of lactose-phospholipid coated $\text{Sm}:\text{CaF}_2$ (i.e., LPL-Sm: CaF_2 , namely paramagnetic glyconanofluorides)

over phospholipid coated $\text{Sm}:\text{SrF}_2$ (i.e., PL-Sm: SrF_2 , and thus referred to as non-glycosylated nanofluorides), in real-time, in the same inflamed tissue by presenting their spatial distribution as a multicolor ^{19}F -MRI map (Figure 3d–i).

In addition to the ability to use them as imaging agents for ^{19}F -MRI, in general, and the potential to use them for multicolor MRI applications in particular (Figure 3), we developed a liquid-state NMR approach with which to study the formation pathways of nanofluorides with a conventional NMR setup, without the need to disturb the reaction conditions. Synthesizing nanofluorides under *in situ* NMR conditions, we were able to probe their sub-nm growth over the entire course of their formation, highlighting their controllable growth mechanisms (coalescence vs. classical simple-growth), which resulted in different morphological and functional features [18, 19]. Examining the correlation between the crystallographic features of the nanofluorides and their relaxation properties, we have developed an approach to shorten the T_1 relaxation times of the fluoride content in nanofluorides by 10-fold only by introducing a defect in their crystals. Such an approach for nanocrystalline-defects relaxation enhancement (NDRE) demonstrates that, while avoiding the use of paramagnetic elements and without introducing the PRE-effect to shorten T_1 values, we were able to extensively enhance the longitudinal relaxation rates of small-sized fluoride NCs to improve ^{19}F -MRI performance [20].

Guest exchange saturation transfer (^{19}F -GEST)

The millimolar sensitivity of ^{19}F -probes restricts the implementation of ^{19}F -MRI to study and map biologically relevant low-concentration targets and calls for novel developments. The maturity of the CEST contrast for MRI [21] opened opportunities to indirectly detect low concentrations of solutes, exploiting both dynamic proton exchange processes and magnetization transfer capabilities. The establishment of the CEST approach created opportunities to implement the CEST principles into ^{19}F -MRI [11, 22] as first demonstrated with fluorinated chelates for sensing and mapping of metal ions [23]. This demonstration of ^{19}F -CEST applicability provided a diverse platform for the development of novel strategies for multicolor MRI. For that purpose, and inspired by the hyperCEST [24] methodology (used with hyperpolarized ^{129}Xe gas as the guest), we developed the ^{19}F -GEST (guest exchange saturation transfer) approach [25–27]. Capitalizing on the different chemical environments of the inner cavity of two different macrocyclic hosts that induce different chemical shift offsets ($\Delta\omega$) of a rapidly exchanging complexed ^{19}F -guest (either upfield or downfield relative to the non-complexed agent), we were able to demonstrate the use of a single ^{19}F -agent for dual-color ^{19}F -MRI with micromolar detectability based on GEST (Figure 4a). Analogously to ^1H -CEST, the large ^{19}F -MR signal of the free ^{19}F -agent mimics the $^1\text{H}_2\text{O}$ signal and the ^{19}F -agent that is bound to the molecular host resembles

the exchangeable proton in ^1H -CEST (compare Figures 1a and 1c). The two different chemical shifts obtained for a bound ^{19}F -agent is a result of the diversity of macrocycles that can be used and the saturation transfer capability is a direct benefit of the reversible dynamic interactions of supramolecular host-guest assemblies that allow the amplification of the ^{19}F -MR signals of extremely low concentrations of complexes.

More specifically, the ^{19}F -agent (or ^{19}F -guest) fluorene is capable of generating significant ^{19}F -GEST contrast in the presence of two different molecular hosts with two opposite $\Delta\omega$ values, either downfield, when incorporated into cucurbit[7]uril (CB7, obtaining a fluorene@CB7 complex), or upfield, when incorporated into octa-acid (OA, obtaining a fluorene@OA complex) relative to the resonance of unbound fluorene (Figure 4b). While the GEST effect of fluorene@OA was at $\Delta\omega = -1.6$ ppm and represented as a green color, the GEST effect of fluorene@CB7 was obtained at $\Delta\omega = 2.2$ ppm and is represented as magenta in the GEST map (Figure 4c–g). Importantly, the existence of either the host or the guest or their complexes does not affect the ^{19}F -MRI appearance and the ^{19}F -GEST contrast is obtained “on demand” upon the application of the saturation pulse at the $\Delta\omega$ of the host-guest complex and can be presented as a dual-colored MRI map (Figure 4e). Note that the ^{19}F -GEST effect can be observed from the intensity of the free ^{19}F -guest at the ^{19}F -NMR spectrum when acquired from a defined voxel using

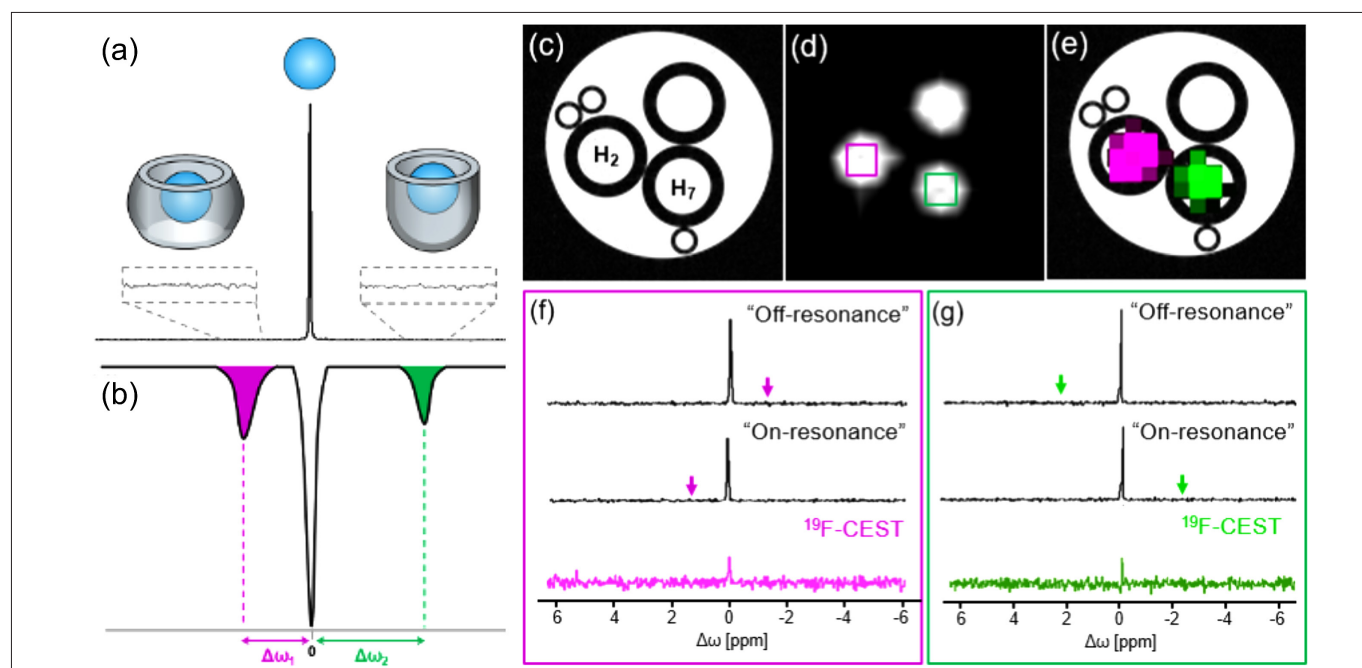


Figure 4. ^{19}F -GEST using host-guest molecular pairs. (a) ^{19}F -NMR spectrum of an aqueous solution of the ^{19}F -guest fluorene (G, 5 mM) and two molecular hosts (50 μM each), CB7 (H_2) and OA (H_7). (b) Schematic z-spectrum representation of an H-G system depicting the opposite GEST effect of a single guest in the presence of two different molecular hosts. (c) ^1H -MRI, (d) ^{19}F -MRI, and (e) ^{19}F -GEST map of 5 mM fluorene and 5 μM of either H_2 (CB7) or H_7 (OA). (f, g) Localized spectroscopy-GEST data of two voxels, as labeled in d.

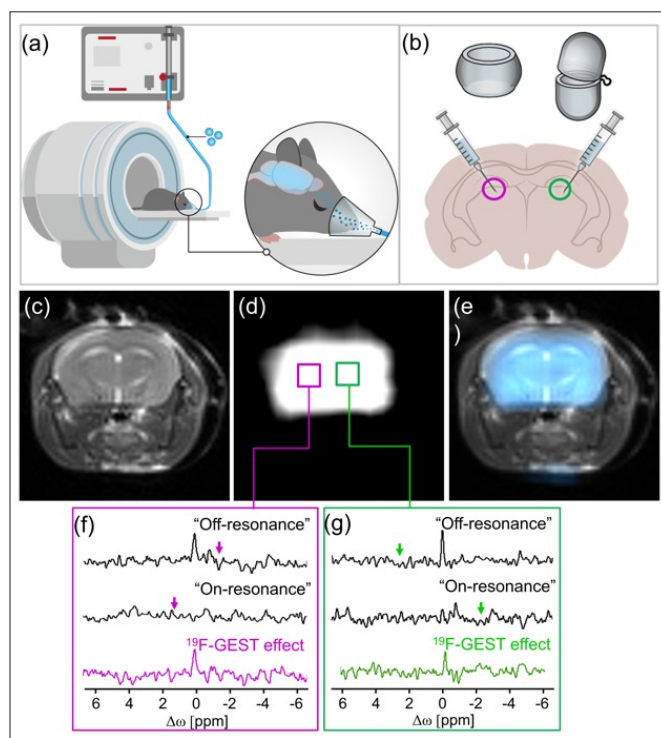


Figure 5. *In vivo* ^{19}F -GEST. (a,b) Schematic illustration of the *in vivo* experimental setup, (c) ^1H -MRI, (d) UTE- ^{19}F -MRI, and (e) ^{19}F -MRI signal overlaid on the ^1H -MRI of a live mouse anesthetized with 4% fluroxene. (f,g) Localized ^{19}F -GEST MRS data.

localized MR spectroscopy (MRS) approaches applied with a pre-saturation pulse at the desired frequencies (Figures 4f,g).

Using a fluorinated anesthetic as an inhalable ^{19}F -guest (i.e., fluroxene), the potential use of ^{19}F -GEST for *in vivo* studies was demonstrated (Figure 5a). To do so, aqueous solutions of either CB7 or OA (in its dimeric form) were delivered intracranially to two opposite hemispheres in the brain of a live mouse (Figure 5b). The examined mouse was then anesthetized with the inhalable ^{19}F -guest fluroxene for the *in vivo* ^{19}F -GEST examination following confirmation of a homogenous distribution of the ^{19}F -guest in the brain with ^{19}F -MRI (Figure 5d–e). *In vivo* localized ^{19}F -GEST MRS (Figures 5f,g) was then performed using two voxels localized at the injection sites of either CB7 (pink square, Figure 5d) or dimeric-OA (green square, Figure 5d) showing the *in vivo* applicability of ^{19}F -GEST through a clear saturation transfer effect observed in the obtained ^{19}F -NMR spectra (Figures 5f and 5g) [28]. This ^{19}F -GEST MR approach offers an alternative strategy with which to detect very low levels of thermally polarized pools of fluorine-19 spins with readily available hardware and may open new avenues for the development of additional molecular architectures for multicolor ^{19}F -MRI, which, so far, has relied on the ability to detect high concentrations of fluorinated pools (Figure 1b).

Despite its potential, even in an *in vivo* setup (Figure 5), the fact that ^{19}F -GEST relies on synthetic organic molecular hosts restricts the values of the $\Delta\omega$ s of incorporated fluorinated guests to a few ppm. This limits not only the number of artificial ^{19}F -GEST colors that can be obtained, but also compromises the spectral resolution of ^{19}F -GEST. To overcome this and expand the number of artificial ^{19}F -GEST colors and enhance ^{19}F -GEST spectral resolution, we proposed a paramagnetic GEST (paraGEST) approach for multiplexed imaging based on paramagnetic supramolecular systems. Inspired by paramagnetic CEST (paraCEST) [29] and the potential to induce pseudo contact shifts (PCSs) to exchangeable fluorinated guests, paraGEST was developed. To do so, we synthesized a library of paramagnetic cavitands based on a lanthanide-cradled α -CD (Figure 6a) and identified a putative fluorinated guest (*para*-trifluoromethyl-benzylamine), which adopts the GEST principles and is capable of producing artificial paraGEST MRI colors (Figure 6b). Establishing an approach we termed CODE-HD (Color Display by Exploiting Host-guest Dynamics), where principles of host-guest binding kinetics with paraCEST and ^{19}F -MRI were combined, we demonstrated a unique approach to generate artificial MRI colors. By inducing PCSs to the chemical shift of dynamically exchanging fluorinated guests in a ^{19}F -NMR framework, which is controlled by the lanthanide element of the paramagnetic host, spectrally resolved artificial colors can be obtained (Figure 6). We demonstrated the versatility of CODE-HD by showing the ability to convert a given color code to another just by replacing the fluorinated guest (and using 3,5-difluorobenzylamine) and enhancing the spectral resolution of the ^{19}F -GEST spectrum as well as enriching the ^{19}F -GEST color palette with additional artificial colors [30]. Such features provide CODE-HD with a convertible color-code capability – a property that is not possible for classical luminescence-based colors or for MRI-based artificial colors.

Proposing GEST ^{19}F -NMR for the study of binding kinetics in a variety of host-guest supramolecular systems, our group demonstrated how this GEST technique, which can be applied using conventional NMR setups, can expand the NMR toolbox currently available to study dynamic host-guest systems in solution without any special expertise or dedicated hardware [31]. Demonstrating the performance of ^{19}F -GEST NMR to study systems composed of cucurbit[n]urils [26, 32], molecular capsules [27], bambusurils [25], cyclodextrins [30], and their mixtures [28] showed its potential to obtain even more artificial MRI colors than those demonstrated above. Nevertheless, although the ^{19}F -GEST MRI provides unique multicolor MRI features that are not applicable in either ^1H -CEST MRI or ^{19}F -MRI, it is important to stress that much more effort is needed before GEST and/or paraGEST are implemented for routine use in imaging setups.

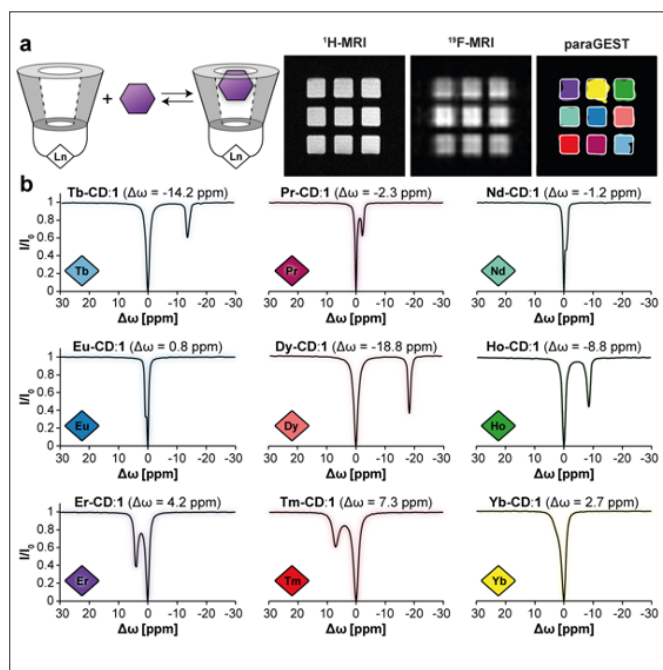


Figure 6. ParaGEST. (a) The dynamic exchange process between a paramagnetic-CD and a fluorinated-guest that allows paraGEST MRI. (b) z-spectra of solutions containing Ln-CD hosts and a ^{19}F -guest. Data were obtained with the fluorinated guest *para*-trifluoromethylbenzylamine. Modified from Reference 30, which is licensed under a Creative Commons Attribution 4.0 International License <http://creativecommons.org/licenses/by/4.0/>.

Genetically engineered reporters for multicolor MRI of gene expression

The revolution of multicolor imaging of multiplex biological systems would not be complete without the development of fluorescent proteins as reporter genes. In this regard, the evolution of the green fluorescent protein (GFP) from its first isolation from the *Aequorea victoria* jellyfish, through the cloning of its gene and its expression as an imageable reporter in cells, to the extension of the fluorescent protein family to a color palette beyond green, has changed science and resulted in the founders being awarded the Nobel prize in chemistry. Realizing the challenges of fluorescent imaging, genetically engineered MRI reporters have been developed as potential alternatives for non-invasive spatial maps of reporter-gene expression [33]. Nevertheless, although extensively developed and demonstrated in multitude animal models, MRI-based reporter-gene signals lack the orthogonal, color-like display capabilities of luminescent reporters. To accomplish multicolor MRI mapping of transgene expression, we aimed to design a set of orthogonal reporter genes that produce multicolor MRI signals that can be spectrally resolved and spatially mapped [34]. To this end, we used a genetically engineered reporter system composed of a reporter gene/

reporter probe pair. More specifically, we capitalized on the vast existing knowledge of a genetically engineered reporter system used in nuclear imaging and composed of a deoxyribonucleoside kinase (dNK) as the reporter gene and synthetic imageable deoxyribonucleoside (dN) as the reporter probe [35, 36].

Our MRI reporter system, which we termed GeneREFORM (stands for GENetically Engineered Reporters FOR multicolor-MRI), is composed of orthogonal reporter probe/reporter gene pairs of dN/dNK. The dN/dNK system relies on the fact that imageable dN is trapped upon its phosphorylation solely in cells engineered to express the heterologous dNK transgene. For GeneREFORM, the synthetic dNs used as the putative reporter probes were the CEST-MRI detectable pyrrolo-deoxycytidine (pdC), a deoxycytidine analog and 5-methyl-dihydrothymidine (5-MDHT), a thymidine analog. Importantly, pdC and 5-MDHT generate CEST contrast from their -NH protons that resonate at $\Delta\omega = 6$ ppm (-NH of pdC) [37] and $\Delta\omega = 5$ ppm (-NH of 5-MDHT) [38, 39], allowing their use as artificial MRI colors in CEST MRI (Figure 7a,b). With the aid of a structure- and evolution-based protein design method, called PROSS [40], followed by active-site-specific mutagenesis of promiscuous dNKs, namely *Dm*-dNK and HSV1-TK, two highly active and fully orthogonal dNKs were developed and obtained. The *Dm*-dNK_7C (PDB Entry - 6YBH) variant was found to be highly active with regard to its ability to phosphorylate pdC with negligible capability

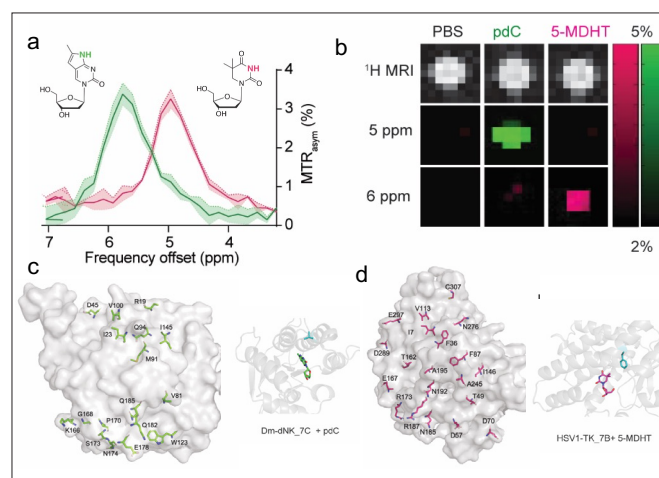


Figure 7. GeneREFORM design. (a) MTR_{asym} plots (i.e., CEST effects representation) of 5-MDHT and pdC emphasizing the negligible level of overlap of CEST peaks. (b) CEST-MRI maps of 5-MDHT, pdC, and PBS solutions obtained at $\Delta\omega = 5$ and 6 ppm. (c) Crystal structure of *Dm*-dNK_7C, presenting its mutations, and inset showing the magnification of the active site with pdC. (d) HSV1-TK_7B structure, presenting its mutations (computational model) and magnification of the active-site vicinity with docked 5-MDHT (right). Modified with permission from Reference 34.

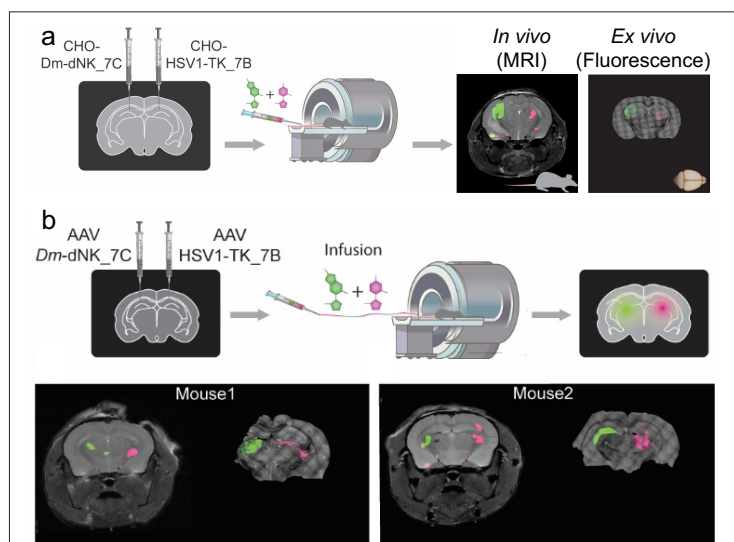


Figure 8. *In vivo* MRI of GeneREFORM. (a) Schematic illustration of the performed *in vivo* study of intracranial injection of transgene-expressing cells, and the CEST maps on an anatomical MR image of the mouse brain. The fluorescent images of a brain cryo-section show the expression of the transgenes. (b) Schematic illustration of the *in vivo* study of intracranial injection of AAV-Dm-dNK_7C and AAV-HSV1-TK_7B in two sets of representative mice showing the CEST maps on an anatomical MR image and the corresponding fluorescent images of a brain cryo-section showing the transgene expression. Modified with permission from Reference 34.

to convert 5-MDHT; and the variant HSV1-TK_7B was confirmed to be a specific dNK for 5-MDHT and not reactive with pdC. Obtaining two highly active and highly orthogonal dN/dNK pairs (pdC/*Dm*-DNK_7C, Figure 7c and 5-MDHT/HSV1-TK_7B, Figure 7d), the molecular components of GeneREFORM were established.

Using these components, we demonstrated the ability to use GeneREFORM to map the simultaneous expression of two different transgenes with MRI in two different animal models. In the first model, tumor cells expressing either of the two transgenes, HSV1-TK_7B or *Dm*-dNK_7C, were inoculated intracranially into the two brain hemispheres of immunodeficient mice. Seven days later, after two contralateral tumors were developed in the brains of this group of mice, a mixture of pdC and 5-MDHT was injected intravenously into the studied subjects. The CEST maps obtained at $\Delta\omega = 5$ and $\Delta\omega = 6$ ppm revealed the accumulation of 5-MDHT or pdC in HSV1-TK_7B- or *Dm*-dNK_7C-expressing cells, respectively, as manifested by the pseudo-colored CEST map display (Figure 8a). A similar observation was obtained when the expression of the orthogonal transgenes was mediated by adeno-associated virus (AAV) vectors (Figure 8b). Overall, we showed, for the first time, the development and implementation of a genetically encoded reporter system, GeneREFORM, that is not based on luminescence and enables

the mapping of transgene expression in a pseudo-multi-color fashion, noninvasively [34].

Summary and outlook

Using synthetic chemistry, supramolecular chemistry, nanofabrication, and protein engineering approaches to generate various types of novel molecular formulations as MRI sensors with unique features, we demonstrated several strategies with which to obtain artificial MRI colors. Having demonstrated the potential of small-sized inorganic nanofluorides to be used as imaging agents for ^{19}F -MRI applications, and considering the extensive use of inorganic NCs for *in vivo* imaging, we envision that further uses of nanofluorides in additional scenarios are just a matter of time. Moreover, the extensive demonstrations of nanofluorides as ideal matrices for NCs with up-conversion fluorescent properties and demonstrations of the use of nanofluorides for CT imaging show the potential to further develop our fluoride-based NCs as materials for multimodal-imaging, beyond multicolor ^{19}F -MRI. The innovative GEST and paraGEST approaches that we have proposed in which host-guest chemistry is combined with ^{19}F -NMR, CEST, and MRI should be further developed to obtain novel molecular systems for molecular and cellular

MRI. While the main challenge in applying GEST-MRI *in vivo* is the need to deliver both the host and the guest to the imaging region, relying on brain-deliverable molecular guests (i.e., fluorinated anesthetics), the potential to modify molecular hosts to recognize biomarkers of neuropathologies (e.g., amyloid-beta plaques in Alzheimer's disease) create opportunities to develop GEST-MRI as a diagnostic tool. Finally, the successful demonstration of the ability to map transgene expression with GeneREFORM, in a pseudo-multi-color fashion, noninvasively, could transform MRI into a powerful tool with capabilities and possibilities that have, to date, been unattainable. GeneREFORM should be further developed to provide additional MRI "colors" and should be applied in developing fields, such as cell-based and gene-based therapies.

In conclusion, there is no doubt that luminescent colors have changed research in the life sciences from the ground up, and, although they are still the obvious choice to illuminate the complexity of biological systems, MRI-based "colors" can extend the available "multicolor" toolbox for scenarios that are not amenable to the use of light. Moreover, and different from other imaging modalities, the information obtained by MRI "colors" can be correlated with other anatomical and physiological parameters that are routinely obtained in MRI studies.

References

1. D. W. Domaille, E. L. Que and C. J. Chang, *Nat Chem Biol*, 2008, **4**, 168-175.
2. N. C. Shaner, R. E. Campbell, P. A. Steinbach, B. N. Giepmans, A. E. Palmer and R. Y. Tsien, *Nat Biotechnol*, 2004, **22**, 1567-1572.
3. X. Gao, Y. Cui, R. M. Levenson, L. W. Chung and S. Nie, *Nat Biotechnol*, 2004, **22**, 969-976.
4. P. Caravan, J. J. Ellison, T. J. McMurry and R. B. Lauffer, *Chem Rev*, 1999, **99**, 2293-2352.
5. A. Bar-Shir, J. W. Bulte and A. A. Gilad, *ACS Chem Biol*, 2015, **10**, 1160-1170.
6. M. T. McMahon, A. A. Gilad, M. A. DeLiso, S. M. Berman, J. W. Bulte and P. C. van Zijl, *Magn Reson Med*, 2008, **60**, 803-812.
7. K. Akazawa, F. Sugihara, T. Nakamura, H. Matsushita, H. Mukai, R. Akimoto, M. Minoshima, S. Mizukami and K. Kikuchi, *Angew Chem Int Ed Engl*, 2018, **57**, 16742-16747.
8. G. Ferrauto, D. Delli Castelli, E. Terreno and S. Aime, *Magn Reson Med*, 2013, **69**, 1703-1711.
9. C. Chirizzi, D. De Battista, I. Tirota, P. Metrangolo, G. Comi, F. B. Bombelli and L. Chaabane, *Radiology*, 2019, **291**, 351-357.
10. U. Flogel, S. Temme, C. Jacoby, T. Oerther, P. Keul, V. Flocke, X. Wang, F. Bonner, F. Nienhaus, K. Peter, J. Schrader, M. Grandoch, M. Kelm and B. Levkau, *Nat Commun*, 2021, **12**, 5847.
11. A. Bar-Shir, N. N. Yadav, A. A. Gilad, P. C. van Zijl, M. T. McMahon and J. W. Bulte, *J Am Chem Soc*, 2015, **137**, 78-81.
12. E. T. Ahrens, R. Flores, H. Xu and P. A. Morel, *Nat Biotechnol*, 2005, **23**, 983-987.
13. U. Flogel, Z. Ding, H. Hardung, S. Jander, G. Reichmann, C. Jacoby, R. Schubert and J. Schrader, *Circulation*, 2008, **118**, 140-148.
14. E. T. Ahrens, B. M. Helfer, C. F. O'Hanlon and C. Schirda, *Magn Reson Med*, 2014, **72**, 1696-1701.
15. I. Ashur, H. Allouche-Arnon and A. Bar-Shir, *Angew Chem Int Ed Engl*, 2018, **57**, 7478-7482.
16. A. Sadoc, M. Body, C. Legein, M. Biswal, F. Fayon, X. Rocquefelte and F. Boucher, *Phys Chem Chem Phys*, 2011, **13**, 18539-18550.
17. D. Cohen, R. Mashiach, L. Houben, A. Galisova, Y. Addadi, D. Kain, A. Lubart, P. Blinder, H. Allouche-Arnon and A. Bar-Shir, *ACS Nano*, 2021, **15**, 7563-7574.
18. R. Mashiach, H. Weissman, L. Avram, L. Houben, O. Brontvein, A. Lavie, V. Arunachalam, M. Leskes, B. Rybtchinski and A. Bar-Shir, *Nat Commun*, 2021, **12**, 229.
19. R. Mashiach, H. Weissman, L. Avram, L. Houben, Y. Diskin-Posner, V. Arunachalam, M. Leskes, B. Rybtchinski and A. Bar-Shir, *Nano Lett*, 2021, DOI: 10.1021/acs.nanolett.1c03131.
20. R. Mashiach, D. Cohen, L. Avram, T. Harris, I. Pinkas, L. Houben, H. Allouche-Arnon and A. Bar-Shir, *Nano Lett*, 2020, **20**, 7207-7212.
21. P. C. van Zijl and N. N. Yadav, *Magn Reson Med*, 2011, **65**, 927-948.
22. A. Bar-Shir, A. A. Gilad, K. W. Chan, G. Liu, P. C. van Zijl, J. W. Bulte and M. T. McMahon, *J Am Chem Soc*, 2013, **135**, 12164-12167.
23. N. D. Tirukoti, L. Avram, T. Haris, B. Lerner, Y. Diskin-Posner, H. Allouche-Arnon and A. Bar-Shir, *J Am Chem Soc*, 2021, **143**, 11751-11758.
24. S. Klippel, C. Freund and L. Schroder, *Nano Lett*, 2014, **14**, 5721-5726.
25. L. Avram, V. Havel, R. Shusterman-Krush, M. A. Iron, M. Zaiss, V. Sindelar and A. Bar-Shir, *Chemistry*, 2019, **25**, 1687-1690.
26. L. Avram, M. A. Iron and A. Bar-Shir, *Chem Sci*, 2016, **7**, 6905-6909.
27. L. Avram, A. D. Wishard, B. C. Gibb and A. Bar-Shir, *Angew Chem Int Ed Engl*, 2017, **56**, 15314-15318.
28. R. Shusterman-Krush, N. D. Tirukoti, A. K. Bandela, L. Avram, H. Allouche-Arnon, X. Cai, B. C. Gibb and A. Bar-Shir, *Angew Chem Int Ed Engl*, 2021, **60**, 15405-15411.
29. M. Woods, D. E. Woessner and A. D. Sherry, *Chem Soc Rev*, 2006, **35**, 500-511.
30. E. Goren, L. Avram and A. Bar-Shir, *Nat Commun*, 2021, **12**, 3072.
31. L. Avram and A. Bar-Shir, *Organic Chemistry Frontiers*, 2019, **6**, 1503-1512.
32. R. Shusterman-Krush, L. Grimm, L. Avram, F. Biedermann and A. Bar-Shir, *Chem Sci*, 2020, **12**, 865-871.
33. A. A. Gilad, K. Ziv, M. T. McMahon, P. C. van Zijl, M. Neeman and J. W. Bulte, *J Nucl Med*, 2008, **49**, 1905-1908.
34. H. Allouche-Arnon, O. Khersonsky, N. D. Tirukoti, Y. Peleg, O. Dym, S. Albeck, A. Brandis, T. Mehlman, L. Avram, T. Harris, N. N. Yadav, S. J. Fleishman and A. Bar-Shir, *Nat Biotechnol*, 2022, **40**, 1143-1149.
35. S. S. Gambhir, E. Bauer, M. E. Black, Q. Liang, M. S. Kokoris, J. R. Barrio, M. Iyer, M. Namavari, M. E. Phelps and H. R. Herschman, *Proc Natl Acad Sci U S A*, 2000, **97**, 2785-2790.
36. J. G. Tjuvajev, G. Stockhammer, R. Desai, H. Uehara, K. Watanabe, B. Gansbacher and R. G. Blasberg, *Cancer Res*, 1995, **55**, 6126-6132.
37. A. Bar-Shir, L. Alon, M. J. Korner, H. S. Lim, N. N. Yadav, Y. Kato, A. P. Pathak, J. W. M. Bulte and A. A. Gilad, *Magn Reson Med*, 2018, **79**, 1010-1019.
38. A. Bar-Shir, G. Liu, M. M. Greenberg, J. W. Bulte and A. A. Gilad, *Nat Protoc*, 2013, **8**, 2380-2391.
39. A. Bar-Shir, G. Liu, Y. Liang, N. N. Yadav, M. T. McMahon, P. Walczak, S. Nimmagadda, M. G. Pomper, K. A. Tallman, M. M. Greenberg, P. C. van Zijl, J. W. Bulte and A. A. Gilad, *J Am Chem Soc*, 2013, **135**, 1617-1624.
40. A. Goldenzweig, M. Goldsmith, S. E. Hill, O. Gertman, P. Laurino, Y. Ashani, O. Dym, T. Unger, S. Albeck, J. Prilusky, R. L. Lieberman, A. Aharoni, I. Silman, J. L. Sussman, D. S. Tawfik and S. J. Fleishman, *Mol Cell*, 2016, **63**, 337-346.